AN ENGINEERING MODEL FOR COAL DEVOLATILIZATION

DOE/PC/88900--5

DE90 003043

Quarterly Report for the Period

March 15, 1989 to June 15, 1989

Grant DE-FG22-88PC88900

Prepared for

THE UNITED STATES DEPARTMENT OF ENERGY

James Hickerson
Project Officer
Pittsburgh Energy Technology Center
Pittsburgh, PA 15236

Submitted by

Mr. Chun Wei Lau and Assistant Professor Stephen Niksa

September 1989

High Temperature Gasdynamics Laboratory
Department of Mechanical Engineering
Stanford University

TABLE OF CONTENTS

1. SUMMARY

There are three distinct modeling projects in this program: (1) An expedient reaction model for coal devolatilization for large scale combustor simulators; (2) A theoretical framework to explain the behavior of different coal types; and (3) An analysis of the chemistry, heat and mass transport in the vicinity of individual coal particles, to begin to describe the initial stages of the combustion of entrained coal particles.

The engineering model was developed before this program began, and has now been validated against several wire-grid studies of HVA bituminous coals. We will resume this task when data from the United Technologies program on coal devolatilization become available.

In a collaboration with Dr. A. R. Kerstein of SNLL, the depolymerization model for coal type effects has been formulated for straight chains, and a simulator is now fully operational. A paper was submitted and accepted for presentation to the upcoming symposium on Coal Pyrolysis Modeling at the ACS National Meeting in Miami in September.

In the third activity, the transport analyses of devolatilizing and oxidizing coal particles, a two-component model which resolves tar and noncondensibles was formulated this quarter, and implemented in a computer simulator; this model is called the AEM3. The flux of tar and noncondensibles is now described with FLASHTWO, our engineering kinetics model.

The AEM3 resolves tar and noncondensibles and illustrates the disparate growth rates of their concentration profiles. Due to its low mass diffusivity, tar tends to remain close to the particle surface throughout devolatilization, while the lighter noncondensible gases penetrate deeply into the free stream. On a molar basis, which is much more relevant to homogeneous oxidation and pyrolysis chemistry, noncondensibles predominate.

The AEM3 simulations also convey interesting implications for ignition mechanisms. Most importantly, resolving the tar and noncondensibles seems to considerable clarify homogeneous ignition mechanisms. The chemical complexity of tar may not be significant because (1) only noncondensibles are present in concentrations greater than typical lean flammability limits; and (2) the noncondensibles contact the hot oxidizer in the far field long before the tar does. Most likely, homogeneous ignition is governed by the noncondensibles in the far field and will be very insensitive to the characteristics of the tar. If this hypothesis proves to be correct, then there are many analyses of ignition in the droplet literature which are pertinent to the homogeneous ignition of coal.

The analysis of heterogeneous ignition can also be clarified somewhat by the AEM3 simulations. When there is no homogeneous chemistry in the vicinity of the particle, blowing during devolatilization cannot exclude inert gases or oxygen from the particle surface. Although the surface oxygen concentration will be diminished by blowing, ignition delays will likely be unaffected. This is because Stefan flow is a small contribution to the total mass flux, even for cases in which the devolatilization rate is artificially increased.

2. INTRODUCTION TO THE PROGRAM

This research program aims for an engineering model for the evolution of volatile products from coal during pulverized coal combustion. The performance specifications include (1) compatibility with the computational constraints of large-scale combustor simulators; (2) reliable predictions of the yields of noncondensible gases, tar, char, and unreacted coal for arbitrary thermal histories and ambient conditions; (3) predictions of the tar molecular weight distribution and aromaticity throughout the technological operating domain; and (4) a mathematical framework for the influence of coal type.

Specifically, this work extends the DISCHAIN and DISARAY models of Niksa and Kerstein to account for the influence of pressure, predict tar molecular weight distributions and aromaticity, and account for the behavior of various coal types. As in the earlier models, the theoretical developments emphasize bona fide depolymerization kinetics and highlight the role of macromolecular configuration in devolatilization behavior. In addition, to account for pressure effects, the theory develops an analogy between the mechanisms for tar evolution and a single-stage, equilibrium flash distillation driven by competitive chemical kinetics.

The program is organized into four tasks. The objective of Task 1 is an engineering model to account for the influence of ambient pressure on the yields and tar molecular weight distributions, including an evaluation against reported devolatilization studies. While the engineering model does not explicitly account for variations in coal type, the theory developed in Task 2 aims for a theoretical framework to handle them. It describes the complete distributions of molecular fragments from a depolymerizing macromolecular network, the reintegration of nonvolatile fragments into a char lattice, and the simultaneous evolution of volatiles by flash distillation. Variations in coal type will be expressed as variations in the structure and composition of the initial network structure.

In Task 3, the engineering model is supplemented with descriptions of the chemistry, heat and mass transport in the vicinity of individual coal particles, to model the initial stages of the combustion of entrained coal particles. In the context of p. c. combustion, the engineering model describes the fluxes of volatiles and energy through the particle surface, while the film models represent volatiles combustion, sooting, and escape. Task 4 emphasizes heuristic treatments of coal type effects developed from the full depolymerization scheme (Task 2), and their evaluation against data.

While there is no in-house experimentation in this program, there is a strong connection to ongoing experimental programs. These models will be evaluated first against wire-grid studies, then against entrained-flow studies as they become available.

3. FINDINGS

During this reporting period, we concentrated on extending our analysis of the transport phenomena in the vicinity of a devolatilizing coal particle. The extended rendition resolves noncondensibles and tars, to characterize the effects of the disparate transport rates for these product lumps. Such resolution is unnecessary for pyrolysis modeling, but will be important in the analysis of the initial stages of combustion.

Only brief status reports are included for the other two activities, beginning in the next section.

3.1 Task 1: An Engineering Model to Account for the Influence of Ambient Pressure on Product Yields and Tar MWD

A draft copy of the final report from the PETC AR&TD Program on Combustion Chemistry was received, courtesy of Dr. Jim Freihaut of UTRC. The extensive representation of various thermal histories will provide stringent tests of dynamic aspects of both the engineering model and the depolymerization theory (FLASHCHAIN). But only two studies are available for coal rank effects, comprising tar yields for a suite of coals heated at 10^3 K/s under vacuum and atmospheric pressure. Total weight loss was not reported, and the coal characteristics do not seem to be tabulated. Any assistance in providing the necessary supporting information from PETC staff will be appreciated.

A more complete set of devolatilization data was reported by Xu and Tomita in Fuel. This set comprises the ultimate yields of tar and all of the important noncondensibles species for atmospheric pyrolysis of 17 coals. For a handful of the coals, the yields are available for several temperatures.

Since we will not be able wait any longer for the PETC AR&TD data base, our data evaluations will emphasize the Xu and Tomita data base, and incorporate Freihaut's wire grid data for high volatile bituminous coals as a means to evaluate thermal history effects.

3.2 Task 2: Detailed Depolymerization Kinetics for the Full Distribution of Fragments from Primary Devolatilization Reactions.

The theory introduced here extends the development of models based on chemical kinetics, macromolecular configuration, and flash distillation, and is called FLASHCHAIN. Like DISCHAIN and DISARAY, it comprises simplified kinetic mechanisms and analytical expressions to account for configurational effects, and to describe their evolution in time. However, the complete size distributions of all fragments are now determined. Due to the complex statistics involved, especially for reattachment, we decided to restrict the

configurational model of coal structure to the nominally infinite linear chain in the first analysis. Coal is obviously not a collection of linear chains but the chain model retains all of the structural components in more complicated lattices, and will be easier to introduce to the research community. Moreover, DISCHAIN, which is based on straight chains, exhibits all of the qualitative features of DISARAY, which is based on the Bethe lattice. Once we understand the behavior of FLASHCHAIN, we will adapt the rate equations to the Bethe lattice.

As demonstrated in the last quarterly, this theory captures the influences of all of the important operating conditions on the devolatilization behavior of high volatile bituminous coals, and in most cases the quantitative agreement is within the experimental uncertainties. These results were put into a form for presentations during the past quarter. A paper was accepted for the upcoming Symposium on Modeling Coal Pyrolysis to be held at the ACS National Meeting in Miami, in September. Another paper has been accepted for the International Coal Science Conference, to be held in Tokyo in October. A manuscript is now being prepared for submission to Energy and Fuels, and will be reported in detail as the next quarterly report.

While the representations of the influences of the operating conditions are encouraging, the theory's greatest potential lies in the formalism to rationalize the behavior of different coals. The data sets discussed in the previous section will be used to evaluate the model's description of coal type, beginning next quarter.

3.3 Task 3: Extensions for Devolatilization During the Initial Stages of Pulverized Coal Combustion

During this quarter, the two-component model was formulated to resolve the disparate transport rates of tar and noncondensible gases. FLASHTWO, our engineering model for the kinetics of primary devolatilization, was substituted for the Distributed-Activation Energy Model, which had been used to predict total volatiles fluxes and transient weight loss in the original AEM. A simulator for the extended model is now fully operational.

The model's derivation follows the motivations in the next section. Then results are presented which show the qualitative features which are common to the AEM and AEM3. The new behavior is then illustrated with several interesting implications for ignition mechanisms, both homogeneous and heterogeneous.

3.3.1 Objectives

The Accumulation Effects Model (AEM) developed previously was our first stepping stone toward an analysis of ignition of individual coal particles. Even though it addressed only heat and mass transfer in the vicinity of a devolatilizing coal particle, it identified one important effect; viz. convective heat transfer rates are substantially enhanced as the thermal profile develops. Once the predicted effect was validated against the measured transient temperatures reported recently by Fletcher at SNLL, it was expressed in terms of an engineering correlation for the transient Nusselt number of non-reacting and reacting particles. All of these effects are described in the manuscript for Combustion and Flame, attached as Appendix I.

All of these results were based on treating the volatile matter as a single species lump. Of course, this ignores the enormous diversity among the actual reaction products, particularly the huge disparity in the mass diffusivities of tars and noncondensible gases. Generally speaking, the time evolution of the concentration profiles of tar and noncondensible gases are governed by their mass diffusivities, and the films grow in proportion to the species diffusion velocity. This omission needs to be rectified, but for rather specific applications.

The single component analysis shows that accumulation effects in the concentration fields are negligible, so that the conventional blowing factor adequately depicts the impact of the outward volatiles flux on the convective heat transfer. Consequently, there is no incentive to resolve the product distribution for the sake of simulated thermal histories or product evolution rates during devolatilization.

However, when oxygen is present, the disparate species transport rates must be distinguished. Flame standoff distances for the noncondensibles will likely be several times larger than for the tars. The growth of the concentration profile of the nonconcondensibles probably governs the ignition mode, either heterogeneous or homogeneous. And throughout most of the product evolution stage, the attached noncondensibles flame will exclude oxygen from its inner core, sustaining the conditions for rapid tar condensation into soot. Fuel nitrogen species expelled from the tar are processed in a thermal profile which is established by the noncondensibles flame.

During the past quarter, a Two-Component Accumulation Effects Model (AEM3) and computer simulator were developed to resolve the disparate transport rates of tars and noncondensible gases. FLASHTWO, our engineering model for the kinetics of primary devolatilization, replaces the Distributed-Activation Energy Model (DAEM), which has been used in the original AEM. This model predicts the evolution rates of tar and

noncondensibles and the tar molecular weight distribution (although only the number-average MW is used in the transport model). Otherwise, as seen in the next section, the formulation of the AEM3 closely follows that of the AEM. Then, after the different growth rates of the two concentration profiles are demonstrated in simulations, parametric studies identify the most important thermophysical properties. Although all of the simulations shown here omit oxygen in the free stream, the AEM3 simulations convey several interesting observations on ignition mechanism.

3.3.2 Mathematical Formulation of the Two-Component Accumulation Effects Model

As in the AEM, there are three assumptions invoked at the outset: First, the particles are spherical throughout and retain their initial size (although their apparent density changes due to the evolution of volatiles, and swelling correlations are easily implemented if available). Second, the concentration and temperature profiles equilibriate rapidly to the changing conditions at the particle surface and at the free stream. Third, internal heat conduction within the particle is relatively rapid (and can be omitted).

Three species are included: tar, noncondensibles as a single product lump, and inert gas. The disparate sizes of these species are represented with only the number average molecular weight of tar, even though the devolatilization sub-model predicts the full MWD.

Mass conservation of various species in the gas film is described by

$$\frac{1}{r^2}\frac{d}{dr}\left(r^2 N_i\right) = 0 \qquad ; \qquad i=1, 2, 3 \tag{1}$$

The radial position in the film is designated by r, which assumes the value 'a' at the particle surface. The χ_i are species mole fractions based on the total vapor concentration C_∞, which is evaluated from the ideal gas law (as P/RT). The N_i are the species molar fluxes. The subscript i designates tars for i=1; noncondensible gases for i=2; and inert gas for i=3. The surface fluxes of the fuel components are specified by FLASHTWO, according to

$$N_1(a) = \left(\frac{a\,\rho_s}{3M_1}\right) R_1^{DEV}$$

$$N_2(a) = \left(\frac{a\,\rho_s}{3M_2}\right) R_2^{DEV}$$

$$N_3(a) = 0 \tag{2}$$

where R_1^{DEV} and R_2^{DEV} are the evolution rates of fractional mass of tars and noncondensibles, respectively, determined independently from FLASHTWO. Note that the first integration of eq. 1 with subsequent application of the surface flux conditions, eqs. 2, expresses the flux at any radial position in terms of the devolatilization rate. Of course, the concentration profile is also of interest.

In a multicomponent system, the molar fluxes are related to the composition gradient by the Stefan-Maxwell equations

$$\frac{d\chi_i}{dr} = \sum_{j=1}^{3} \frac{1}{C_\infty D_{ij}} (\chi_i N_j - \chi_j N_i) \qquad ; \qquad i=1, 2, 3 \tag{3}$$

The very dense coupling in eq. 3 will be unraveled shortly. Note especially that only two of these equations are independent, because the mole fractions sum to unity by definition. Also, in the most rigorous formulation for multicomponent transport, multicomponent diffusivities are used for each component. These parameters are not available for most species, and such resolution is certainly not appropriate in this model, because of its coarse definition of the reaction species. We implement the Chapman-Enskog relations to introduce a simple parameterization for the disparate diffusivities.

The disparate diffusivity in this reference frame is that for tars in inert and tars in noncondensibles, which is related to D and is assumed to be the same, according to

$$D_{12} = D_{13} = D, \text{ the reference diffusivity for the system}$$

Because of their similar molecular weights, noncondensibles and inerts are assigned the same transport characteristics and is related to that of tars with a multipicative constant, γ, so that

$$D_{23} = \gamma D$$

In actuality γ is a parameter that depends slightly on temperature, but it will be treated as a constant because the uncertainty in the magnitude of D is much greater than the expected temperature dependence. Incorporating the Chapman Enskog approximations considerably simplifies the Stefan-Maxwell equations, yielding the form

$$N_1 = -C_\infty D\frac{d\chi_1}{dr} + \chi_1 \sum_{i=1}^{3} N_i$$

$$N_2\left[(\gamma - 1)\chi_1 + 1\right] = -C_\infty \gamma D\frac{d\chi_2}{dr} + \chi_2\left[(\gamma - 1)N_1 + \sum_{i=1}^{3} N_i\right]$$

$$N_3\left[(\gamma - 1)\chi_1 + 1\right] = -C_\infty \gamma D\frac{d\chi_3}{dr} + \chi_3\left[(\gamma - 1)N_1 + \sum_{i=1}^{3} N_i\right] \qquad (4)$$

Nondimensional forms of these relations use a new radial coordinate, $\xi = a/r$, and the following scale factors for the fluxes:

$$P_1 \equiv \frac{N_1(a)}{(DC_\infty/a)}$$

$$P_2 \equiv \frac{N_2(a)}{(\gamma DC_\infty/a)} \qquad (5)$$

We choose the diffusive scale because the inverse r-squared weighting in the Stefan flow restricts its influence to the immediate vicinity of the particle surface. Note that the sum of the two non-dimensional surface fluxes, P_1 and P_2, does not equal to the total volatiles surface flux, P_v as defined in the One-Component AEM. This is because in AEM3, different diffusive scales are needed for each fuel component to determine the different extents of the concentration profiles. But in the original AEM, there is only a single fuel component and hence a single diffusivity. The relation among the three scaled surface fluxes involves γ, and is

$$P_v = \frac{P_1}{\gamma} + P_2 \qquad (6)$$

The mathematical model is completed with the additional stipulation that the mole fractions of both fuel species vanish at the outer edge of the film, $\chi_1 = 0$ at $\xi_1^\infty = 0$ and $\chi_2 = 0$ at $\xi_1^\infty = 0$. As in the original AEM, the species fluxes were expressed in terms of the surface fluxes and the transformed radial coordinate, then eliminated from the Stefan-Maxwell relations. The remaining set of three coupled, first order, ordinary differential equations can still be solved analytically for the concentration profiles, which are

$$\chi_1 = \left(\frac{P_1}{\gamma P_v}\right)\left[\,1 - \exp(-\gamma P_v\,(\xi - \xi_1^{\infty}))\right]$$

$$\chi_2 = \left(\frac{P_2}{P_v}\right)\left[\,1 - \exp(-(P_1 + P_2)\,(\xi - \xi_2^{\infty}))\right]$$

$$+ \left(\frac{P_1}{\gamma P_v}\right)\left[\exp(-\gamma P_v\,(\xi - \xi_1^{\infty})) - \exp(-\gamma P_v\,(\xi_2^{\infty} - \xi_1^{\infty}))\,\exp(-(P_1 + P_2)(\xi - \xi_2^{\infty}))\right] \quad (7)$$

The concentration profiles depend on the scaled instantaneous devolatilization rates, P_1, P_2, and P_v, and the extents of both concentration profiles, ξ^{∞}_i, which are finite in value. Of course, since the transport rates of both fuel components differ, the extents of the respective concentration profiles must be distinguished. The equations that govern the time evolution of the two concentration film thicknesses, ξ^{∞}_1 and ξ^{∞}_2, are developed later in this section.

The analysis of the temperature profile in the film is similar. Energy conservation in the gas phase ensures that

$$\frac{1}{r^2}\frac{d}{dr}(r^2 e) = 0 \quad (8)$$

where

$$e \equiv -\lambda_g \frac{dT_g}{dr} + \sum_{i=1}^{3} N_i H_i$$

The total enthalpy flux, e, represents the redistribution of enthalpy by both i) molecular conduction, so the thermal conductivity, λ_g, and the gradient of the gas temperature, T_g, appear, and also by ii) the Stefan flow field. In this latter contribution, H_i is the species molar enthalpy, which is evaluated as the product of a species mean heat capacity, C_{pg}, and the difference between the gas and reference temperature, $(T_g - T_r)$.

The temperature profile, subject to the condition that the film temperature relaxes to the free stream condition at the outer boundary ($T_g(\xi^{\infty}_T) = T_\infty$), and to the instantaneous particle temperature at the inner boundary ($T_g(a) = T_s$), is given by

$$T_g = T_s + (T_\infty - T_s)\left[\frac{\exp\left(-\frac{\varepsilon}{Le}(\xi - 1)\right) - 1}{\exp\left(-\frac{\varepsilon}{Le}(\xi^\infty_T - 1)\right) - 1}\right] \qquad (9)$$

where

$$\varepsilon \equiv \frac{P_1}{\gamma}\beta_1 + P_2\beta_2$$

$$\beta_1 \equiv \frac{C_{p1}}{C_{pg}} \quad ; \quad \beta_2 \equiv \frac{C_{p2}}{C_{pg}}$$

$Le = \lambda_g/C_{pg}\gamma DC_\infty$, the Lewis number of the gas mixture.

The temperature profile depends on the nondimensional surfaces fluxes, P_1, and P_2, the instantaneous particle surface temperature, T_s, and the nondimensional thermal film thickness, ξ^∞_T, which changes in time. Note that a solution for an infinite film obtains by evaluating the profile at $\xi^\infty_T = 0$.

The interphase heat flux to the particle is proportional to the thermal gradient of the gas temperature at the particle surface, $(-dT_g/dr)$, which can be evaluated from the instantaneous temperature profile. The interphase heat flux through the surface affects the rate of change of the particle temperature with time, as do the rates of radiant transfer and convection of sensible enthalpy through the surface as tars and noncondensible gases escape. In addition, the reaction endotherm accounts for the energy required to vaporize the volatile products. Consequently, the energy balance for the particle is

$$\rho_s C_s l_p \frac{dT_s}{dt} = \sigma\varepsilon_p(T_w^4 - T_s^4) + \lambda_g \left.\frac{dT_g}{dr}\right|_{r=a} + (N_1(a) + N_2(a))\,\Delta H_p \qquad (10)$$

where

ρ_S = bulk density of the coal particle, kg/m^3

C_s = specific heat of the fuel, J/kg-K

l_p = volume to surface ratio, m

σ = Stefan-Boltzmann constant, $W/m^2\text{-}K^4$

ε_p = particle emittance

T_w = wall temperature or effective radiant collection temperature, K

ΔH_p^i = pyrolysis endotherm for species i, J/mole

To close the mathematical system, we define the thicknesses of both of the species profiles and of the thermal profile in relations which ensures that the total exchange of mass and energy between the particle and the gas phase are conserved. That is, mass accumulation in the film is proportional to the mass flux through the surface, according to

$$4\pi a^2 N_1(a) = \frac{d}{dt}\int_a^{r_1^\infty} 4\pi r^2 C_\infty \chi_1(r)\, dr \tag{11}$$

$$4\pi a^2 N_2(a) = \frac{d}{dt}\int_a^{r_2^\infty} 4\pi r^2 C_\infty \chi_2(r)\, dr \tag{12}$$

where C_∞ is a mean molar concentration evaluated at a mean temperature defined by the one-third rule. The unknown species film thicknesses, $r^\infty{}_1$ and $r^\infty{}_2$, appear as the limit of integration.

Similarly, the global energy balance requires that

$$4\pi a^2\left[-\lambda_g \frac{dT_g}{dr}\bigg|_{r=a} + N_1(a)H_1(T_s) + N_2(a)H_2(T_s)\right] =$$

$$\frac{d}{dt}\int_a^{r_T^\infty} 4\pi r^2 C_\infty \left[\sum_{j=1}^{3}\chi_j H_j(T_g) - H_3(T_\infty)\right] dr \tag{13}$$

where $H_3(T_\infty)$ is the molar enthalpy of the inert gas at the free stream temperature. Here also the dependent variable, $r^\infty{}_T$, appears as the limit of integration.

Using the same conduction time scale and temperature scale as defined in the One-Component AEM, the nondimensional time and temperatures in the AEM3 are defined as

$$\tau \equiv \frac{3\lambda_g t}{\rho_s C_s a^2} \quad ; \quad \theta_i \equiv \frac{T_i - T_o}{T_r - T_o} \tag{14}$$

Introducing these scales, and the previously defined profiles of gas film temperature and species concentration fields, eqs. 10-12 can be rendered nondimensional as follows

Particle Energy Balance:

$$\frac{d\theta_s}{d\tau} = \left[\frac{\frac{\varepsilon}{Le}}{\exp\left(\frac{\varepsilon}{Le}(\xi_T^{\infty} - 1)\right) - 1} \right](\theta_{\infty} - \theta_s) + \bar{Q}_r + \left(\frac{P_1}{\gamma} + P_2\right)\Delta\bar{H}_p \tag{15}$$

$$\theta_s(0) = \frac{T_s(0) - T_o}{T_r - T_o}$$

where

$$\bar{Q}_r \equiv \frac{a\sigma\varepsilon_p T_W^4}{\lambda_g \Delta T}\left[\left(\frac{\theta_s + (T_o/\Delta T)}{\theta_w + (T_o/\Delta T)}\right)^4 - 1 \right]$$

$$\Delta\bar{H}_p \equiv \frac{\Delta H_p}{Le\, C_{pg}\, \Delta T}$$

$$\Delta T \equiv T_r - T_o$$

Global Mass Balances:

$$P_1(\tau) = \left(\frac{t_d}{t_c}\right)\frac{d}{d\tau}\int_{\xi_1^{\infty}}^{1} \frac{\chi_1(\xi)}{\xi^4}\, d\xi \tag{16}$$

$$P_2(\tau) = \frac{1}{\gamma}\left(\frac{t_d}{t_c}\right)\frac{d}{d\tau}\int_{\xi_2^{\infty}}^{1} \frac{\chi_2(\xi)}{\xi^4}\, d\xi \tag{17}$$

where

$$\frac{t_d}{t_c} = \frac{3\,Le\,C_{pg}\,C_\infty}{\rho_s C_s}$$

Global Energy Balance:

$$\left[\frac{\frac{\varepsilon}{Le}}{\exp(\frac{\varepsilon}{Le}(\xi_T^\infty - 1)) - 1}\right](\theta_s - \theta_\infty) + \frac{P_1}{\gamma}\bar{H}_1(\theta_s) + P_2\bar{H}_2(\theta_s) =$$

$$\left(\frac{t_d}{t_c}\right)\frac{d}{d\tau}\int_{\xi_T^\infty}^{1}\frac{\left[\sum_{j=1}^{3}\chi_j\bar{H}_j(\theta_g) - \bar{H}_3(\theta_\infty)\right]}{\xi^4}\,d\xi \qquad (18)$$

where

$$\bar{H}_j \equiv \frac{H_j}{Le\,C_{pg}\,\Delta T} = \frac{\beta_j}{Le}\theta_g$$

The primary outcome of the formulation is a set of four integro-differential equations (eqs. 15-18) for the four time dependent variables ξ^∞_1, ξ^∞_2, ξ^∞_T, and T_s. The integral relations were made more tractable for numerical simulation by evaluating the derivatives of the integrals, to define the time-derivatives of the film thickness in terms of various quadratures. Numerical results are presented in what follows, after we show that the two-component model subsumes the original AEM in an appropriate limit.

3.3.3 Relating the One and Two-Component Formulations

The relation between the AEM and AEM3 is evident in their formulations. Obviously, the formulations are very similar, and all of the basic premises and assumptions are the same. Qualitatively, very similar behavior can be expected of both models. In this section, the similarities are emphasized by identifying the appropriate limiting conditions in which the AEM3 collapses to the AEM. Then, in following sections, new performance aspects during transient heating are demonstrated.

In the AEM simulations reported previously, particle heating rates were significantly enhanced during the initial stages of transient heating, while the thermal profile was developing. Later, during devolatilization, the convective heat transfer rate fell dramatically as convection was suppressed by the outward flow of volatile matter. While accumulation effects cause the initial enhancement of heating rates, they are inconsequential during blowing; in fact, Nusselt numbers during devolatilization from the AEM for simulated p. f. firing conditions are indistinguishable from those based on the conventional blowing factor.

The first accumulation effect, which enhances heating rates, is independent of the species concentration profiles because it is usually complete before the onset of product evolution. There are reacting systems in which product evolution coincides with the development of a thermal profile, but coal devolatilization is not one of them. Even at heating rates as large as 10^5K/s, devolatilization commences at 800K or higher, so the thermal profile is almost fully developed by the time blowing begins. Consequently, the initial enhancement of heating rates is independent of the concentration profiles from either the AEM or AEM3. During devolatilization, blowing does impede the inward flux of energy, but nevertheless remains insensitive to the transient evolution of the concentration profile. That is why the conventional blowing factor closely mimics the behavior of the AEM, and why with AEM3, the segregation of volatiles into tars and noncondensible gases does not affect the predicted impact of blowing.

These similar qualitative features can be brought into a more formal context, by identifying the limiting conditions in which the AEM3 is reduced to the AEM. The appropriate limit is expressed in terms of identical mass diffusivities for tars and noncondensible gases, for which $\gamma = 1.0$.

Simply setting $\gamma = 1.0$, and $\xi^{\infty}_1 = \xi^{\infty}_2 = \xi^{\infty}_s$, in the AEM3 reduces the concentration and temperature profiles to

$$\chi_1 = \left(\frac{P_1}{P_v}\right)\left[1 - \exp(-P_v(\xi - \xi_s^{\infty}))\right] \tag{19}$$

$$\chi_2 = \left(\frac{P_2}{P_v}\right)\left[1 - \exp(-P_v(\xi - \xi_s^{\infty}))\right] \tag{20}$$

$$T_g = T_s + (T_{\infty} - T_s)\left[\frac{\exp\left(-\frac{P_v}{Le}(\xi - 1)\right) - 1}{\exp\left(-\frac{P_v}{Le}(\xi_T^{\infty} - 1)\right) - 1}\right] \tag{21}$$

The temperature profile is the same as in the AEM. Summing the two species concentration profiles recovers the concentration profile as the single product lump in the AEM, since $P_1 + P_2 = P_V$ if $\gamma = 1$.

3.3.4 Physical Properties

The physical properties used in the AEM3 simulations which follow are shown in Table I. The specific heat of coal is that reported by Merrick [1], and includes a strong temperature dependence. The heat capacity of non-condensible gases are taken as that for ethylene, which has a very molecular weight to the average for the noncondensible volatiles.

The heat capacity of tar is much more uncertain. Conservative bounds were developed from group additivity of linear aliphatics and condensed aromatics, as seen in Fig. 1. For number average molecular weights consistent with values based on GPC in pyridine reported by Oh, of about 300 g/g-mole, the heat capacity is bounded between 80 and 115 cal/mole-K. The simulations are based on the nominal average of about 100.

The thermal conductivity of the gases is assigned based on simple additivity in proportion to the respective mole fractions, but will be extended with Wilke additivity. The base value of the diffusivity of the tar is assigned coarsely to that of a heavy PAH compound, but varied widely in parametric studies. The pyrolysis endotherm (which is inconsequential) is assigned from Freihaut's estimate and literature survey [2]. The emittance of coal is based on recent measurements at SNLL [3].

3.3.5 Simulation Results

The first simulations create a context for the behavior of the AEM3 with reference to that of the AEM. One of the cases used in the presentation of the AEM is recomputed with the AEM3 in Fig. 2. The operating conditions are for Haussman's experiments with 55 μm HVA bituminous coal particles injected into a gas stream at 1400 K. Thermal histories from the AEM3 appear as the solid curve for comparison with those from the AEM and our original Nusselt number correlation, shown as dashed and dotted curves, respectively.

The temperatures from the AEM3 rarely deviate by more than 10K from those from the AEM, so they are also well represented by the correlation. The predicted mass loss and product evolution rates are also in close agreement for the three cases. These results suggest that the Nusselt number correlation developed from the AEM can also depict the initial predictions from the AEM3, but we were unable to implement this strategy because of numerical stability problems. The computational time for the AEM3 is substantial, in that the results in Fig. 2 required about two hours of run time on a 20MHz, 386-type personal microcomputer.

TABLE I
Thermophysical Properties used in AEM5

COAL

PSOC 1451 Coal

Mean Diameter, μm	55.0
Apparent Density, g/cm^3	1.2
ASTM Volatiles Matters, wt%(as rec'd)	34.5
Ultimate Volatiles Yield, wt%(d.a.f.)	46.6
Swelling ratio(γ), %	0.0
Emissivity	0.7
Pyrolysis Endotherm(ΔH_p)[2], cal/g	100.0

Specific heat of the fuels: temperature-dependent correlation of heat capacities for coal developed by Merrick[1].

GAS MIXTURE

Specific heat of tars: 100 J/mole-K

Specific heat of noncondensibles: 42 J/mole-K

Specific heat of O_2 : 32.2 J/mole-K

Specific heat of Ar : 21 J/mole-K

Average MW of noncondensibles(M_{nc}): 25 g/mole

Average MW of tars(M_{tar}): as evaluated by FLASHTWO for the time increment.

Mass diffusivity for tars: 6.43 x 10^{-6} m^2/s

Chapman-Enskog coefficient, γ: 30

Thermal Conductivity for the gas mixture: 0.0451 W/m-K

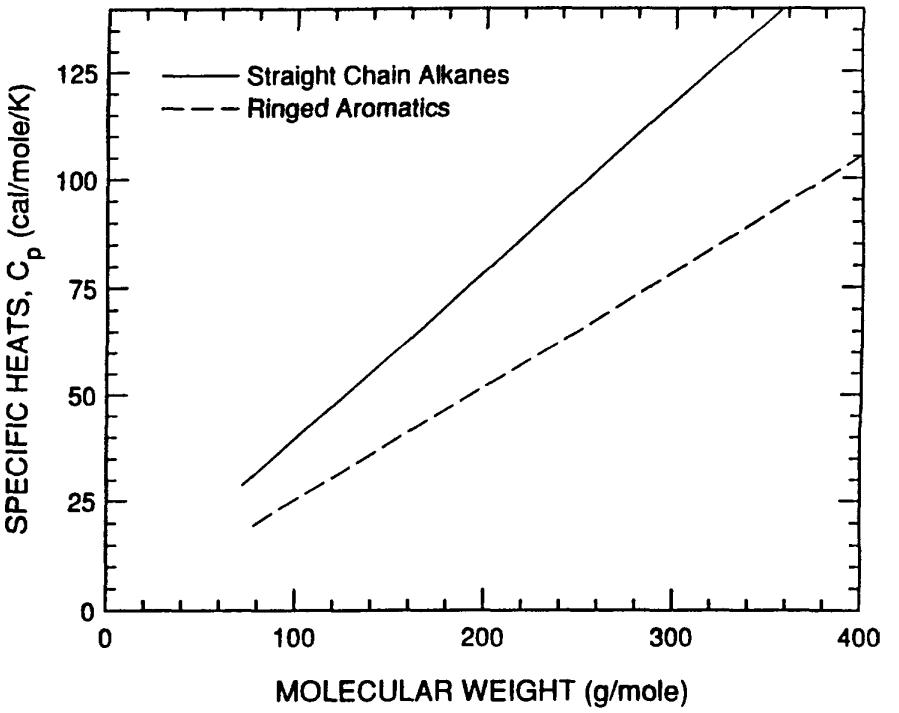

Figure 1. Bounds on specific heat at constant pressure estimated by functional group addivity for hydrocarbons at T = 300 K.

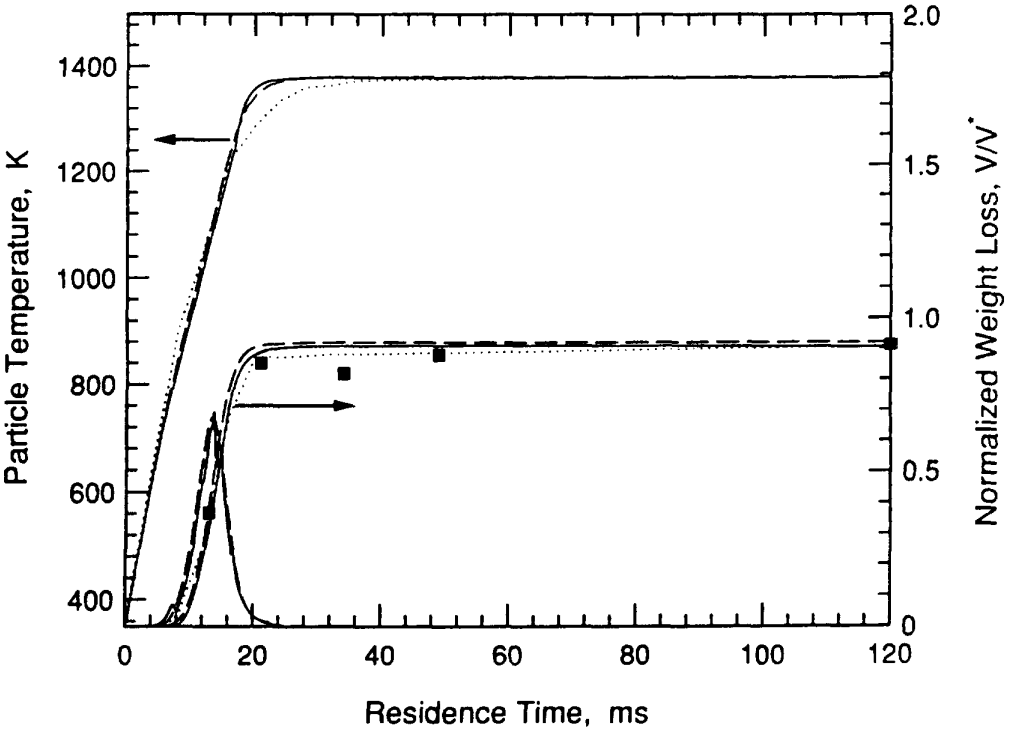

Figure 2. Comparison of particle temperature and weight loss histories evaluated by AEM(--), AEM5(—) and the Nusselt No. correlation in [1] (....). The scaled aggregate volatiles fluxes from the AEM(--) and AEM5(—) are also shown. Gas and effective radiant collection temperature are 1400 and 900K, respectively; particle diameter is 55 mm (no oxygen).

In the AEM3, the flux of volatiles through the particle surface is based on FLASHTWO [4]. Rate parameters for FLASHTWO are collected in Table 2. They were assigned by matching the transient weight loss and the scaled instantaneous volatiles flux, P, with those predicted by the DAEM using the parameters in the original AEM simulations. We use the behavior of the earlier model as the standard for its replacement because it was validated against the weight loss profiles for heating rates from 0.5 to about 10^5K/s. As seen in Fig. 2, the scaled instantaneous devolatilization rate, P, and the transient weight loss evaluated with FLASHTWO (solid curve) and the DAEM (dashed curve) are nearly the same. Since the thermal history from the correlation is so similar to the others, the agreement among all of the predicted devolatilization rates and yields is not surprising.

TABLE II
KINETIC PARAMETERS FOR FLASHTWO

Bridge dissociation rate:

$$A_{ob} = 3.0 \times 10^{10}$$

$$E_{ob} = 40 \text{ Kcal/mole}$$

$$\sigma_{ob} = 4.5 \text{ Kcal/mole}$$

Char Formation rate:

$$A_{oc} = 4.5 \times 10^{12}$$

$$E_{oc} = 45 \text{ Kcal/mole}$$

A new feature from the AEM3 is demonstrated in Fig. 3, as the predicted evolution of the extents of the thermal, noncondensible gas, and tar concentration profiles; operating conditions are the same as in Fig. 2. These quantities represent the transformed radial positions at which the free-stream conditions are applied throughout the process. Three separate cases are shown for the tar film thickness, using various values of the ratio of the diffusivities of noncondensibles and tar. Note also that the proportions of tar and gas from FLASHTWO with the parameters in Table 2 are in accord with product distributions reported recently for HVA bituminous coals (although they are not shown).

There are several interesting features. First, the thermal field develops before the onset of product evolution. By the time products are generated, at about 4 ms, the thermal film has grown to about 10 particle diameters. Consequently, the blowing factor will closely

approximate the effect of blowing on the interphase heat transfer. The coupling between product evolution and the heat transfer involves only the aggregate flux of sensible energy, so resolving the contributions from tar and noncondensibles is unimportant. Consequently, there is no incentive to refine the estimates of the thermophysical properties of coal tar for this analysis. The results in Fig. 3 also show that, throughout devolatilization, the thermal film contains both concentration films.

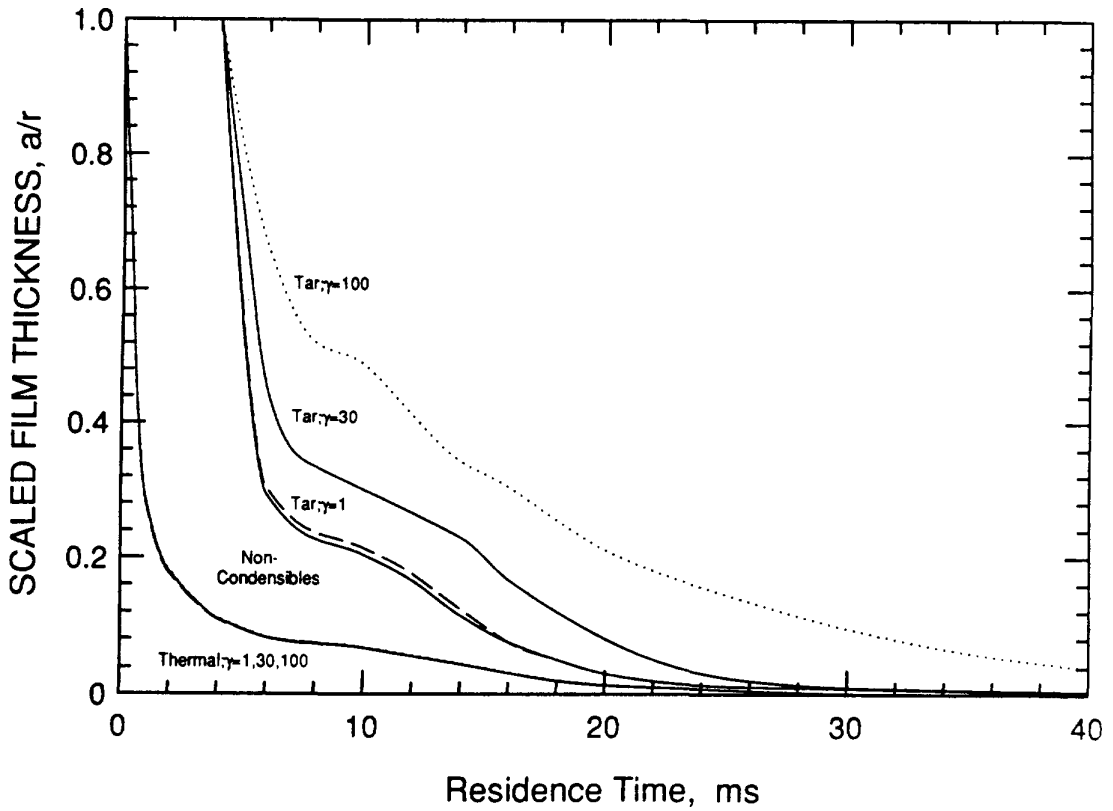

Figure 3. Comparison of the nondimensional film thicknesses for temperature and tar and noncondensibles composition for various values of γ: 1 (--), 30 (—) and 100 (....). Same operating conditions as in Fig. 1.

Second, only for the case of equal diffusivities for tar and noncondensibles do the concentration profiles develop at the same rate. For non-unity values of γ, the noncondensibles film develops faster. At 10 ms, with γ equal to 30, the tar and noncondensibles profiles extend to 3 and 5 diameters, respectively; with γ = 100, the respective thicknesses are 2 and 5 diameters. Because of the disparity in the diffusivities of tar and noncondensibles, the noncondensibles film will always contain the tar profile. Clearly these simulations pave the way for the more interesting case where the noncondensibles ignite into a flame which envelops the tar and sustains its pyrolysis.

Once devolatilization is over, at about 20 ms, all profiles continue to develop with diminishing gradients and nominally infinite extents.

The computed concentration profiles of tar and noncondensibles appear in Fig. 4 at about 14 ms, when the devolatilization rate is at a maximum, and at 18 ms, when it is just about over. Clearly tar is restricted to the immediate vicinity of the particle surface until the later stages. These results also convey the large disparity of the species concentrations on a molar basis. Such small amounts of tar are present that, again, there is little incentive to refine its thermophysical properties. Only its diffusivity is important in these simulations.

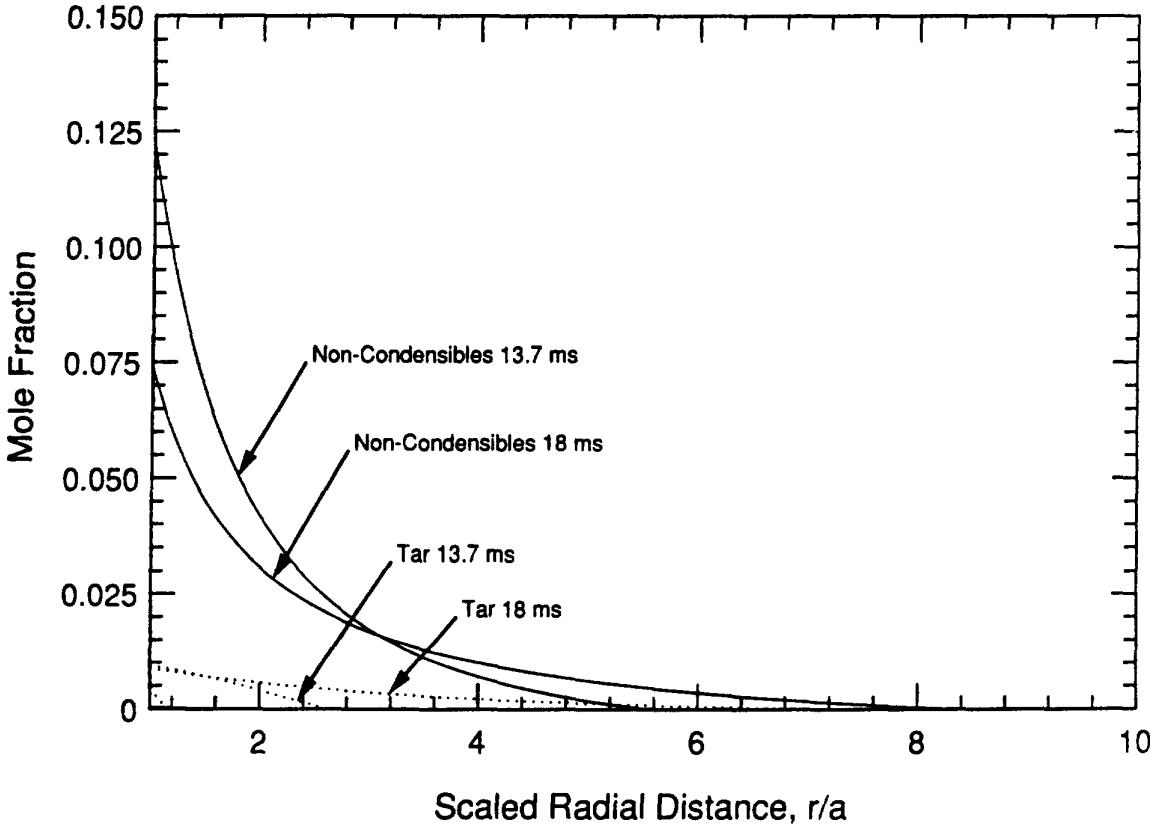

Figure 4. Concentration profiles of noncondensibles (—) and tar (....) at 13.7 ms, when the devolatilization rate is at a maximum, and at 18 ms, near the end of devolatilization.

The relative impact of the Stefan flow and Brownian diffusive flux for the aggregate volatiles is shown in Fig. 5 at various reaction times. As expected, Stefan flow is most important when the devolatilization rate is maximized, at about 14 ms. Yet even here, Stefan flow is a relatively minor contribution, accounting for only about one-eighth of the total mass flux. The important implication is again on ignition, but this time for the heterogeneous

mechanism. Given the small contribution of Stefan flow, the effect of blowing on the mass transfer is not comparable to its effect on heat transfer. It is particularly clear that blowing cannot exclude oxygen from the particle surface; in fact, in these simulations inert gases are analogous to oxygen, because of their similar molecular weights, and the surface mole fraction of inerts is always large (and given by unity minus the mole fraction of volatiles). When homogeneous chemistry is absent, oxygen will be able to reach the particle. Although its surface concentration will be diminished by blowing, it will not be excluded.

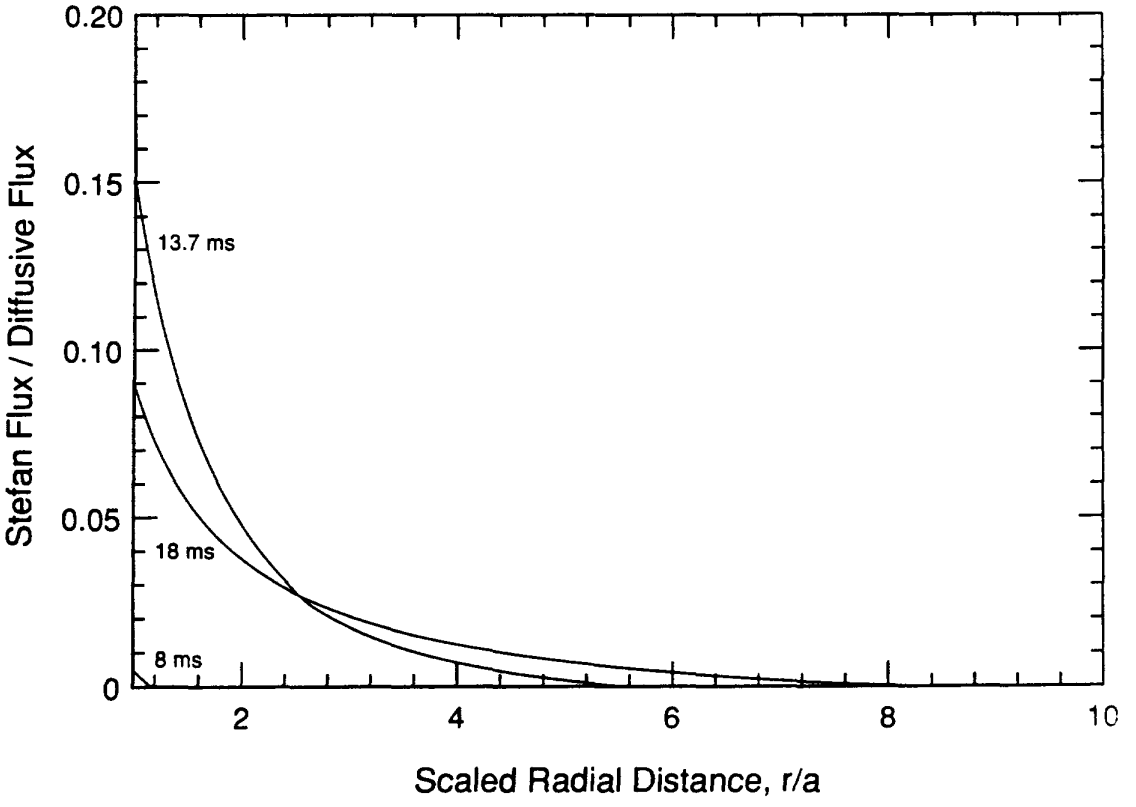

Figure 5. The ratio of the stefan flux to the brownian diffusive flux at the peak (13.7 ms) and near the end of devolatilization (18 ms).

This conclusion was investigated further by artificially enhancing the Stefan flux. By narrowing the standard deviation about the mean activation energy in the bridge dissociation rate, the same extent of devolatilization is forced to occur in a narrower temperature interval: hence, the same products are forced to escape in shorter time, and the volatiles flux is substantially increased. The predictions for a single bridge dissociation energy (i.e., sigma equal zero) appear in Fig. 6 along with the results for the base case discussed above; the particle temperature history, transient normalized weight loss and scaled devolatilization rate, P, are included.

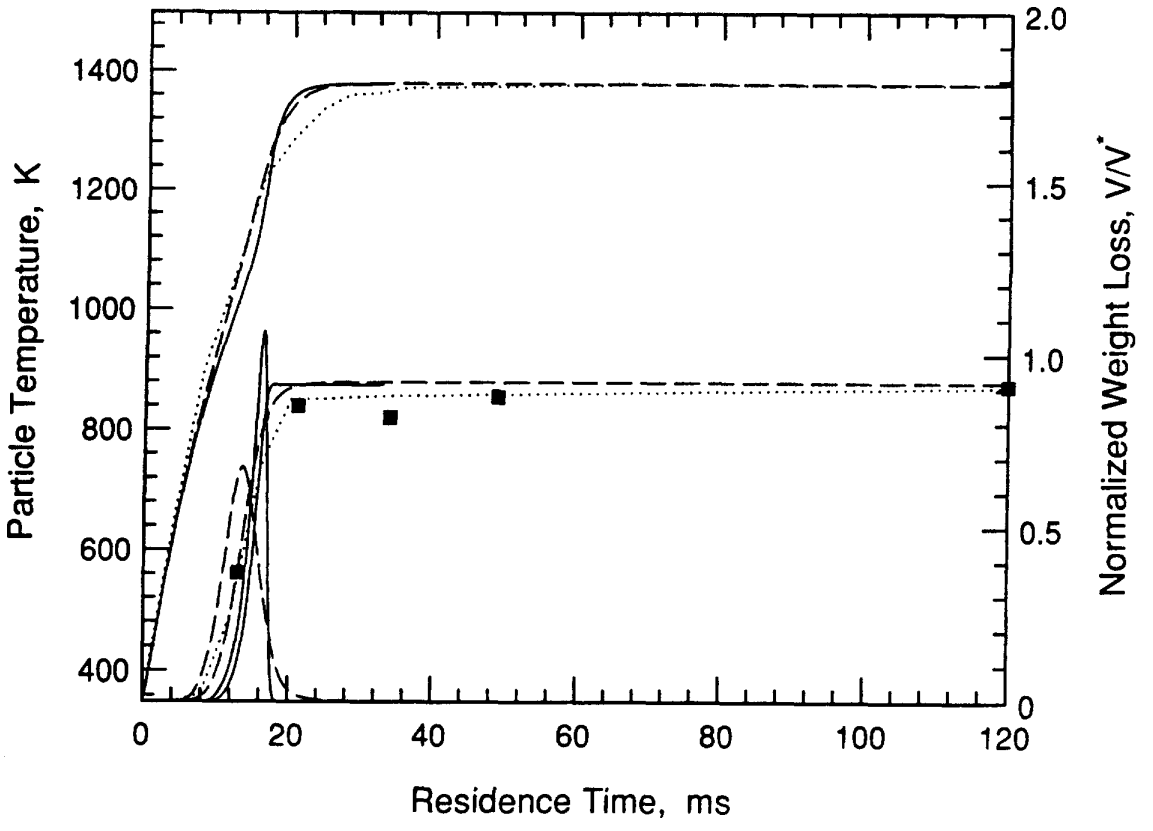

Figure 6. Comparison of particle temperature and weight loss histories evaluated by AEM(--), AEM5(—) and the Nusselt No. correlation in [1] (....). The scaled aggregate volatiles fluxes from the AEM(--) and AEM5(—) are also shown. These predictions are based on a single bridge dissociation energy(i.e. σ=0). The operational conditions are the same as in Fig. 1.

The maximum devolatilization rate is observed later than in the base case, at about 16 ms. Note especially that the peak rate has grown by about 75%, which is probably beyond the plausible limit for any coal. Consequently, the transient mass loss develops quicker, and the perturbation in the thermal history due to blowing is exaggerated.

But the impact on the surface mole fraction remains too small to exclude any gas in the free stream from the particle surface. In Fig. 7, the contribution from Stefan flow is seen to increase over the base case, as expected, but remains relatively minor. Even when the devolatilization rate is nearly doubled, Stefan flow accounts for only about 20% of the total mass flux.

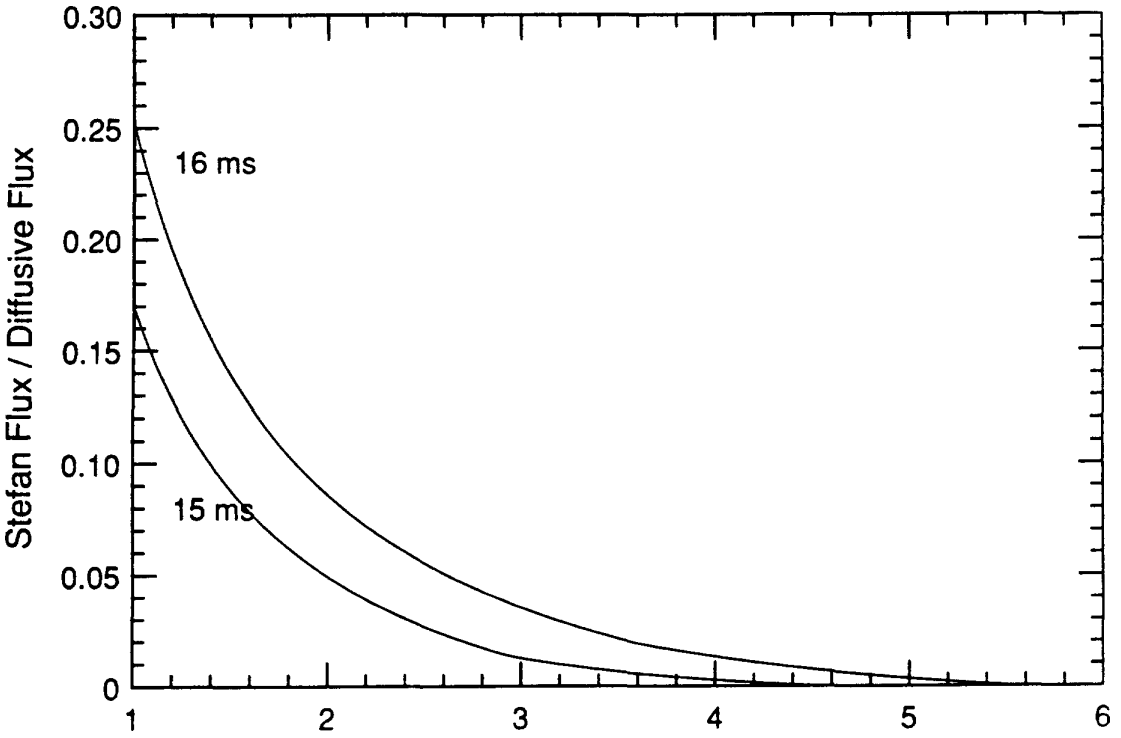

Figure 7. The ratio of the stefan flux to the brownian diffusive flux at the peak (16 ms) and near the peak of devolatilization (15 ms) based on a single bridge dissociation energy(i.e. σ=0).

3.3.6 Conclusions

The AEM3 resolves tar and noncondensibles and illustrates the disparate growth rates of their concentration profiles. Due to its low mass diffusivity, tar tends to remain close to the particle surface throughout devolatilization, while the lighter noncondensible gases penetrate deeply into the free stream. On a molar basis, which is much more relevant to homogeneous oxidation and pyrolysis chemistry, noncondensibles predominate.

The simulations convey interesting implications for ignition mechanisms. Most importantly, resolving the tar and noncondensibles seems to considerable clarify homogeneous ignition mechanisms. The chemical complexity of tar may not be significant because (1) only noncondensibles are present in concentrations greater than typical lean flammability limits; and (2) the noncondensibles contact the hot oxidizer in the far field long before the tar does. Most likely, homogeneous ignition is governed by the noncondensibles

in the far field and will be very insensitive to the characteristics of the tar. If this hypothesis proves to be correct, then there are many analyses of ignition in the droplet literature which are pertinent to the homogeneous ignition of coal.

The analysis of heterogeneous ignition can also be clarified somewhat by the AEM3 simulations. When there is no homogeneous chemistry in the vicinity of the particle, blowing during devolatilization cannot exclude inert gases or oxygen from the particle surface. Although the surface oxygen concentration will be diminished by blowing, ignition delays will likely be unaffected. This is because Stefan flow is a small contribution to the total mass flux, even for cases in which the devolatilization rate is artificially increased.

4.0 SHORT TERM OBJECTIVES

The new devolatilization theory, FLASHCHAIN, will be examined for parametric sensitivity, with an emphasis on coal type effects. Systematic ways to relate the model parameters to coal characteristics will be devised by fitting the Xu and Tomita data set. We will also prepare a manuscript on the formulation of the theory and its satisfactory depiction of the influences of the operating conditions for submission to Energy and Fuels. Also, paper on FLASHCHAIN will be presented at the Symposium on Coal Pyrolysis Modeling at the ACS National Meeting in Miami.

The transport analysis will be extended to included oxygen penetration to the surface and heterogeneous combustion. Since the Stefan flow can only diminish, not exclude, oxygen from the surface, these simulations will gauge the impact on ignition delays and temperatures.

5.0 REFERENCES

1. Merrick, D.: Fuel **62**, p. 533 (1983).

2. Freihaut, J.D., "A Numerical and Experimental Investigation of Rapid Coal Pyrolysis," Ph.D. thesis, Department of Material Science and Engineering, Penn. State University, May 1980.

3. Fletcher, T.H., "Time-Resolved Particle Temperature and Mass Loss Measurement of a Bituminous Coal during Devolatilization," paper presented at the Fall Meeting, the Western States Section/The Combustion Institute, Dana Point, CA, Oct. 1988.

4. Niksa, S.: AIChE Journal, p. 790, AIChE, May 1988.

Nomenclature

a	Radius of the particle, m
C_{pg}	Mean heat capacity of the gas mixture, J/mole-K
C_s	Heat capacity of the particle, J/kg-K
C_∞	Molar concentration of the gas mixture, mole/m^3
D	Diffusivity of the tars, m^2/s
D_{ij}	Diffusivity of the pair i-j in a binary mixture, m^2/s
e	Energy flux with respect to the stationary coordinates, J/m^2.s
H_i	Entahlpy of species i, J/mole
$\bar{H}_i$	Scaled enthalpy of species i, J/mole
Le	Lewis number
l_p	Volume to surface ratio, m
M_i	Molecular weight of species i, kg/mole
N_i	Molar flux relative to a stationary coordinate of species i, mole/m^2
P_i	Scaled devolatilization strength for species i
$\bar{Q}_r$	Scaled radiant energy flux
r	Radial coordinate, m
R_i^{dev}	Evolution rate for species i, mole/s
T	Temperature, K
T_g	Gas mixture temperature, K
T_o	Reference temperature, K
T_r	Free stream reactor temperature, K
T_s	Particle temperature
T_w	Reactor wall temperature or effective radiant collection temperature, K
T_∞	Far field gas temperature
t	Dimension time, sec.

Subscripts

g	refer to value of a variable in the gas phase
i	refer to the species i
o	refer to the reference condition
r	refer to the reactor condition
s	refer to value of a variable at the particle surface
T	refer to the thermal field
w	refer to the radiant wall condition
∞	refer to the far field of the outer boundary condition
1	refer to tars
2	refer to noncondensibles
3	refer to inert gas

Superscripts

∞ refer to value of a variable at the outer boundary
dev refer to devolatilization chemistry

Greek Letters

β_i ratio of heat capacity of species i to the mean gas mixture heat capacity
ϵ_p Emissivity of the particle
σ Stefan-Bolztman constant
λ_g Thermal conductivity of the gas mixture, W/m.K
γ Chapman-Enskog coefficient for binary mass diffusivities
θ Dimensionless temperature
θ_g Dimensionless gas mixture temperature
θ_s Dimensionless particle temperature
ρ_s Solid particle initial density, Kg/m^3
τ Dimensionless time as defined in text
τ_c Particle convective heating time, sec.
τ_d Gas phase characteristic diffusion time, sec.
ξ Dimensionless radial co-ordinate, a/r
ξ_i^∞ Dimensionless layer thickness for species i
ξ_T^∞ Dimensionless thermal layer thickness
χ_i Mole fraction of the i^{th} component in the gas mixture

preprint removed. da